PIER C

A Novel Direct Instantaneous Torque Control Strategy of Permanent Magnet-Assisted Switched Reluctance Motor with Zero Voltage Modulation

Chaozhi Huang, Renquan Xiao*, Chengyi Gong, and Yong Xiao

School of Electrical Engineering and Automation, Jiangxi University of Science and Technology, Ganzhou 341000, Jiangxi, China

ABSTRACT: To reduce large torque ripple in permanent magnet-assisted switched reluctance motors (PMa-SRMs), a novel direct instantaneous torque control (DITC) strategy with zero-voltage modulation is proposed in this paper, where a fixed-frequency pulse width modulation (PWM) is replaced by the conventional DITC hysteresis controller to optimize zero-voltage insertion time through zero-voltage decentralized modulation to minimize switching losses. Control intervals are then divided based on inductance and torque-to-current ratio (TCR) characteristics, with adaptive duty cycle adjustments to enhance torque tracking and reduce ripple. Additionally, the optimal turn-on and turn-off angles are determined by the dung-beetle-optimized back propagation (BP) neural network (DBO-BP) algorithm, which suppresses the torque ripple, lowers phase current peaks, and improves motor efficiency. The feasibility and effectiveness of the proposed method are validated by simulations and experiments with a three-phase 6/20 PMa-SRM.

1. INTRODUCTION

PMa-SRM not only has the advantages of simple structure, low cost, and high reliability but also has higher power density and efficiency, larger TCR, and high application potential than conventional switched reluctance motors [1–3]. However, the double-convex pole structure of SRM stator-rotor also causes a high degree of nonlinearity in electromagnetic characteristics, which in turn tends to cause a series of problems such as large torque ripple and low system operating efficiency, thus limiting the application and development of SRMs [4, 5]. Therefore, researchers have proposed a series of improvement measures to suppress torque ripple and improve the operating efficiency of SRMs.

In terms of control strategies, commonly used methods include direct torque control (DTC) [6], torque sharing function control (TSFC) [7], PWM control [8], and DITC [9]. To suppress torque ripple in SRM, [10] introduces a real-time optimized DTC method that adjusts based on real-time differences between observed and reference magnetic flux and torque values. Ref. [11] replaces hysteresis control with a fuzzy controller to improve torque tracking by analyzing errors between reference and measured torque. DTC requires a large amount of magnetic chain and torque characteristic data to support control operations. Due to the lack of regulation of the turn-on and turn-off angles, the motor can generate significant negative torque during operation, which affects its efficiency. In [12], a nonuniform TSF control method with an adaptive overlap angle is proposed, which partitions control interval according to the inductive characteristics to optimize the TSF curve shape and parameters. In [13–15], an online TSFC method, which en-

hances current tracking capability through a novel online current profile generation technique and commutation angle optimization, is introduced. These methods effectively reduce torque ripple, peak currents, and copper losses.

DITC is widely utilized to drive motors through rotor position, torque error, and hysteresis control schemes. However, the nonlinear inductive characteristics have a significant effect on torque ripple. Refs. [16–18] address the large torque ripple in the commutation zone caused by conventional DITC's single control strategy, which neglects variations in phase winding torque with rotor position. They propose dividing the commutation region, designing separate hysteresis schemes, and optimizing turn-on and turn-off angles using an algorithm. To enhance SRM efficiency, [19] introduces a new online phase change optimization strategy. This approach uses zonal control based on the motor's TCR, constructs an objective function from efficiency and torque ripple coefficients, and optimizes boundary angles with a genetic algorithm. However, the hysteresis control method, which suffers from variable switching frequency and high noise, has been largely replaced by fixed-frequency voltage PWM modulation. In [20], the PWM duty cycle is adjusted based on torque error to regulate the winding voltage, somewhat affecting torque ripple suppression. However, this method incurs high switching losses. In [21–23], PWM control is used instead of hysteresis in conventional DITC to manage torque deviation. By selecting optimal switching signals based on PWM modulation and rotor sector, this approach effectively reduces both torque ripple and switching losses.

This paper proposes a novel DITC method with zero-voltage modulation to address the uncontrollable switching frequency

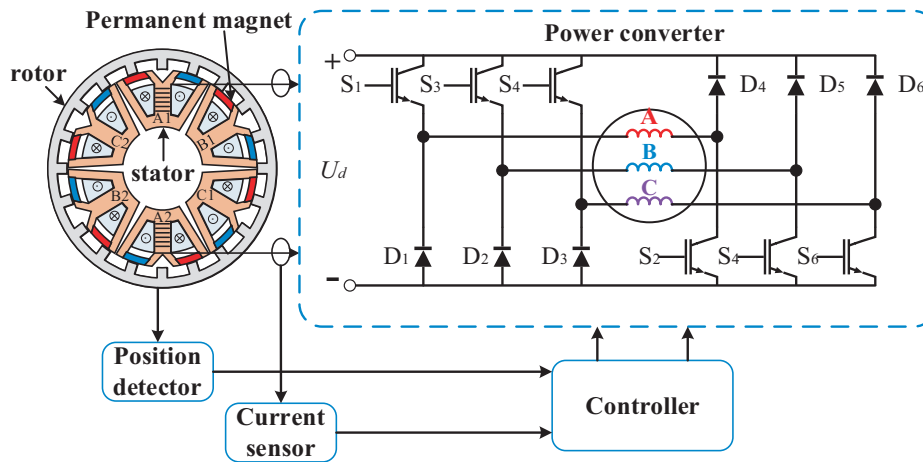* Corresponding author: Renquan Xiao (1762058847@qq.com).
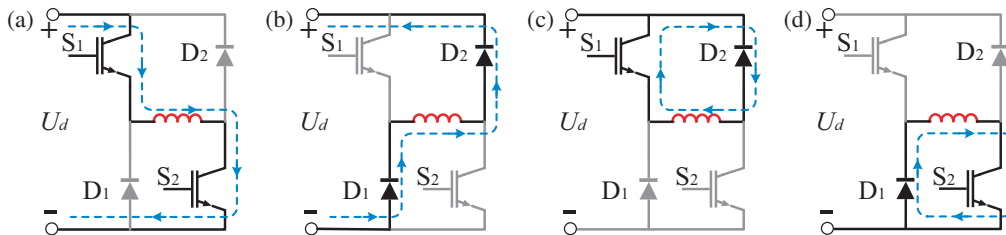
71

FIGURE 1. PMa-SRM drive system.

FIGURE 2. Switching states of the circuit. (a) Excitation state. (b) Demagnetization state. (c) Freewheeling state 1. (d) Freewheeling state 2.

of conventional DITC. A fixed-frequency PWM waveform is used for zero-voltage decentralized modulation to reduce switching loss. Meanwhile, to suppress torque ripple in the phase change region, interval adaptive duty cycle control is performed based on inductance and TCR characteristics. Additionally, to adapt to varying operating conditions, turn-on and turn-off angles are optimized using DBO-BP to reduce torque ripple and improve motor efficiency. Finally, the effectiveness of the proposed method is validated through simulation and experimentation.

2. CONTROL AND ANALYSIS OF PMA-SRM DRIVEN SWITCHES

2.1. PMa-SRM Speed Control System

The basic structure of the 6/20-pole PMa-SRM speed control system is shown in Fig. 1, which is mainly composed of five parts: PMa-SRM, controller, power converter, position detector, and current sensor. A, B, and C are the three-phase windings of the motor; S_1–S_6 are switching tube Insulated Gate Bipolar Transistors (IGBTs); and D_1–D_6 are freewheeling diodes. Among them, asymmetric half-bridge power converter (AHBC) is the most commonly utilized power conversion circuit in an SRM drive system, and its operating states can be divided into the excitation state "S = 1", demagnetization state "S = −1", and zero-voltage freewheeling state "S = 0" as shown in Fig. 2. There are two types of freewheeling states: when S_1 is on and S_2 off, the phase winding is freewheeling

through S_1 and D_2; when S_1 is off and S_2 on, the phase winding is freewheeling through S_2 and D_1.

The voltage balance equation for a phase winding during PMa-SRM operation is given by

$$u_j = i_j R_j + \frac{d\psi_j}{dt} = i_j R_j + L_j(\theta, i_j)\frac{di_j}{d\theta} + i_j\omega_j\frac{dL_j(\theta, i_j)}{d\theta} \quad (1)$$

where $u_j, i_j, \psi_j, L_j, w_j$, and θ are phase voltage, phase current, magnetic chain, inductance, speed, and rotor position angle, respectively.

SRM operates with the flux always following the path of minimum reluctance. Neglecting the magnetic saturation effect, it can be deduced from the electromechanical linkage equation that the electromagnetic torque can be expressed as:

$$T_j = \frac{1}{2}i_j^2\frac{dL}{d\theta} \quad (2)$$

2.2. Conventional DITC Strategy

The conventional DITC control method is based on the error between the actual output torque T_e^* of the PMa-SRM and its given reference torque T_{ref}, and the control signals of each phase are output through the torque hysteresis controller. The schematic diagram of a conventional DITC system, as depicted in Fig. 3, consists of an inner torque loop and an outer speed loop. Its control system comprises an instantaneous torque estimation unit, hysteresis controller, proportional-integral (PI) controller, position sensor, and power converter.
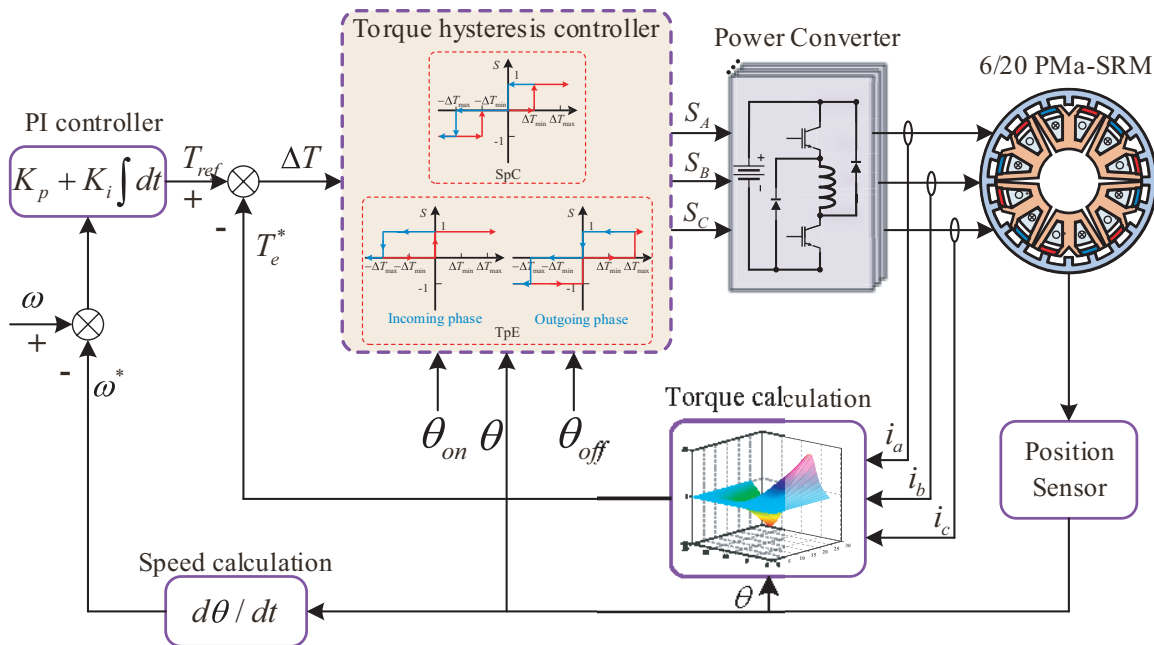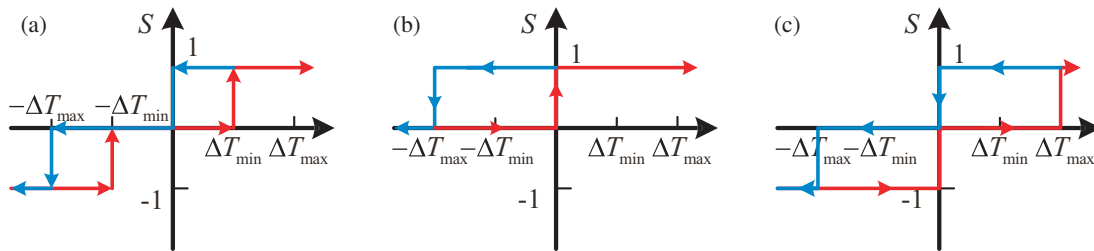
FIGURE 3. Block diagram of conventional DITC system.

FIGURE 4. Conventional DITC hysteresis rule. (a) SpC region. (b) TpE region incoming phase. (c) TpE region outgoing phase.

The conventional DITC strategy is divided into two regions based on inductance characteristics: two-phase switching region (TpE) and single-phase conduction region (SpC). Its hysteresis rules are shown in Figs. 4(a), (b), and (c). $\Delta T_{\min}$ and $\Delta T_{\max}$ are the inner and outer hysteresis band thresholds, respectively, and S denotes the switching state. The torque error is defined as

$$\Delta T = T_{ref} - T_e^* \qquad (3)$$

where ΔT, T_{ref}, and T_e^* indicate torque error, reference torque, and instantaneous torque, respectively.

To suppress torque ripple, hysteresis control typically follows these principles: During the SpC region, torque is primarily provided by the conducting phase, with phase switching modified according to torque error. As shown in Fig. 4(a), priority in phase conduction alternates between excitation and freewheeling modes to prevent severe torque ripple caused by entering demagnetization states. In TpE region, torque is regulated jointly by the incoming and outgoing phases. From Figs. 4(b) and (c), it is evident that the primary task of the incoming phase is to establish phase currents rapidly, with switching states predominantly between 1 and 0. The outgo-ing phase's main function is rapid demagnetization to prevent negative torque generation.

In TpE region, the conventional DITC strategy's hysteresis control rules do not fully account for changes in inductance characteristics. As a result, the outgoing phase may remain active, leading to significant negative torque and reduced motor efficiency. Meanwhile, due to the double hysteresis control, determining the switching frequency is arduous, leading to larger torque ripple and increased switching loss. Furthermore, in instances of speed and load alterations, the fixed conduction angle could intensify the motor's torque ripple and exacerbate the issue of excessive peak current.

3. PROPOSED CONTROL STRATEGY

This paper improves conventional DITC by addressing several issues. First, it uses fixed-frequency PWM and a new modulation mode to cut switching losses. Second, it adapts the duty cycle across different intervals based on TCR characteristics to adjust the voltage at both ends of the winding. Third, DBO-BP is used to optimize the conduction angle, reducing torque ripple and peak current to improve system efficiency. Fig. 5 shows the
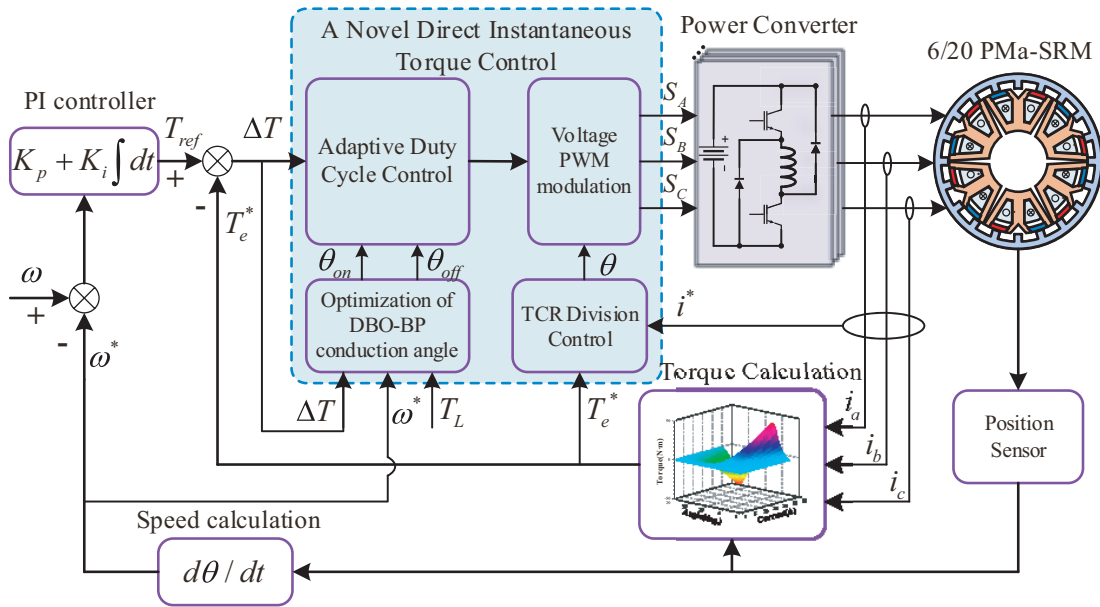
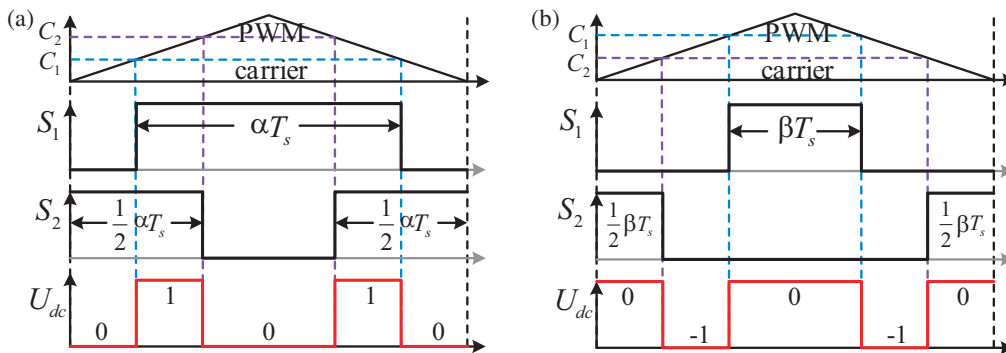**FIGURE 5**. Block diagram of a novel DITC with zero-voltage modulation.

FIGURE 6. The proposed PWM modulation method. (a) Voltage signal waveform during excitation of phase winding. (b) Voltage signal waveform during phase winding demagnetization.

block diagram of the updated DITC system with zero-voltage modulation.

3.1. Control Signal Type Improvement

PWM control, also known as voltage chopper control, regulates the voltage at both ends of the winding by adjusting the modulation and duty cycle. Its fixed control frequency allows for more flexible changes in voltage and torque, and it can effectively improve control accuracy.

To generate appropriate control signals, this paper employs a zero-voltage decentralized modulation strategy, as depicted in Fig. 6. A triangular carrier wave varying within the range of $[0, 1]$ is compared with modulation signals C_1 and C_2 to generate control signals for switches S_1 and S_2. The comparison values C_1 and C_2 are quantitatively related to the duty cycle D, all within the range of $[0, 1]$. For switch S_1, a middle-duty cycle modulation method is employed: when the carrier wave value exceeds the comparison value C_1, switch S_1 conducts;

otherwise, S_1 is turned off. For switch S_2, a two-end duty cycle modulation method is used: when the carrier wave value is less than C_2, switch S_2 conducts; otherwise, S_2 is turned off. Within one control cycle, the two modulation methods maintain identical duty cycles, which are applied to achieve an average voltage range of $[-U_{dc}, U_{dc}]$ for a phase.

The phase winding excitation and demagnetization output voltage signal waveforms are shown in Figs. 6(a) and 6(b), where α and β are the respective duty cycle sizes. At this time, α is greater than 0.5, β less than 0.5, and T_s for the control cycle.

3.2. Interval Dividing

The phase inductance of the PMa-SRM can be expressed as a function of current and rotor position, as illustrated by the inductance characteristic curve in Fig. 7. The magnitude of phase inductance varies not only with rotor position but also with current magnitude. The rate of change of phase inductance exhibits
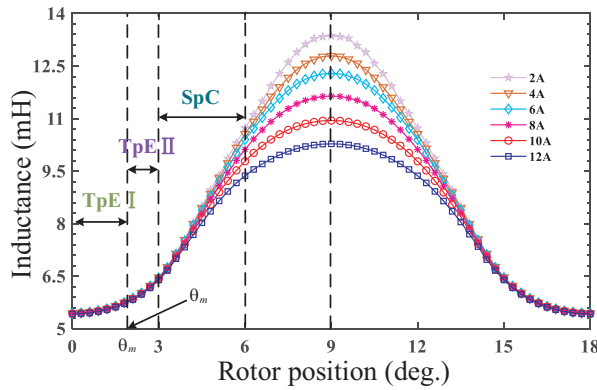
FIGURE 7. Inductance curve.

periodic variation with rotor position, as indicated by Equation (2), and the torque output capability per phase is similarly influenced by rotor position. Under constant current conditions, a higher rate of inductance change corresponds to greater torque output capability per phase. Therefore, based on the different torque output capabilities of each phase winding at various rotor positions, control intervals are delineated accordingly.

From Equation (2), it can be deduced that the TCR is

$$TCR = \frac{T_j}{i_j} = \frac{1}{2} i_j \frac{dL}{d\theta} \qquad (4)$$

When the phase current is constant, the TCR is determined by the ratio of phase inductance to rotor position. The three-phase TCR characteristic curves relative to rotor position are depicted in Fig. 8. Here, 0° and 9° represent the incoming phase rotor misalignment and alignment positions, respectively, with 3° indicating the phase lead alignment position, and the range from 0° to 3° being the commutation zone. Based on the characteristics of adjacent phase TCRs, the commutation zone can be subdivided into two sub-intervals, with the boundary point of the
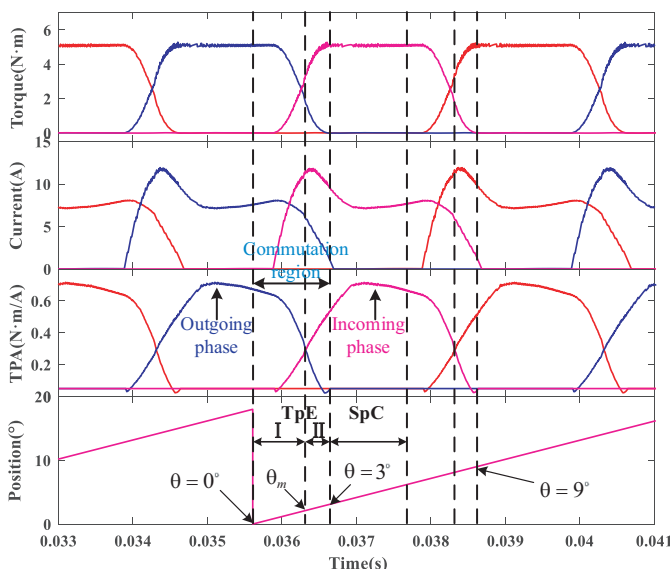

FIGURE 8. TCR characteristics.

interval being θ_m where the two phase TCRs are equal. From Fig. 8, it can be observed that between 0° and θ_m, the TCR of the outgoing phase surpasses that of the incoming phase, indicating a greater torque generation capability for the outgoing phase than the incoming phase. Therefore, this region is designated as TpE I. Between θ_m and 3°, the TCR of the incoming phase exceeds that of the outgoing phase, signifying a stronger torque generation capability for the incoming phase. Hence, this region is defined as TpE II. Between 3° and 6°, the inductance rises linearly, and the TCR remains constant, which defines the SpC region.

The winding voltage $U_j = D U_s$ is regulated by the PWM duty cycle, and the phase winding resistance is disregarded. The rate of current change can be deduced from formula (1):

$$\frac{di}{d\theta} = \frac{U_j - i\frac{dL}{d\theta}\omega}{\omega L} \qquad (5)$$

From Equation (5), it can be seen that the rate of change of current is related to the voltage at both ends of the winding, inductance and speed. If the same duty cycle is used throughout the conduction interval, torque ripple suppression is suboptimal. Therefore, the duty cycle is adaptively adjusted based on speed and load to regulate the voltage action time at both ends of the winding. The control block diagram is shown in Fig. 9.
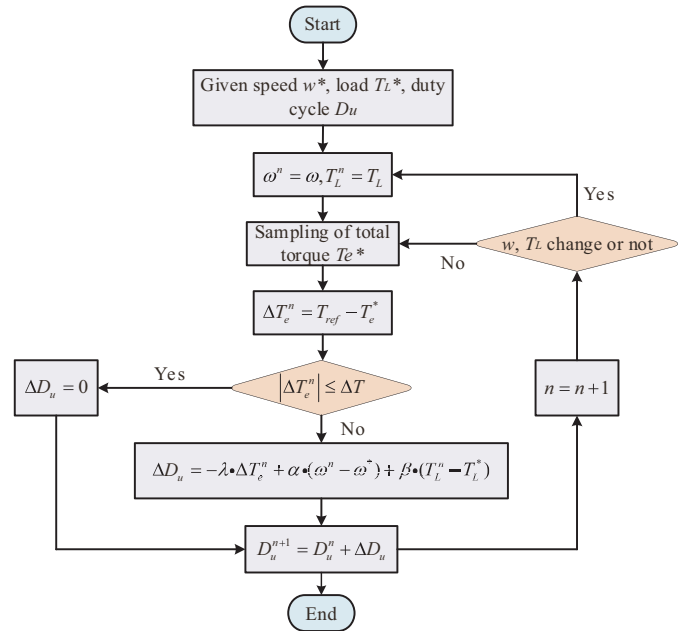

FIGURE 9. Adaptive duty cycle control.

3.3. Conduction Angle Optimization

According to the torque and inductance characteristics of PMa-SRM, positive torque output occurs when the rate of inductance change is greater than zero; conversely, negative torque output occurs when the rate of inductance change is less than zero. The commutation angle significantly influences motor efficiency and torque ripple throughout the commutation process. Fig. 10 illustrates the phase current variation with rotor position under different turn-on and turn-off angles. Here, i^* represents
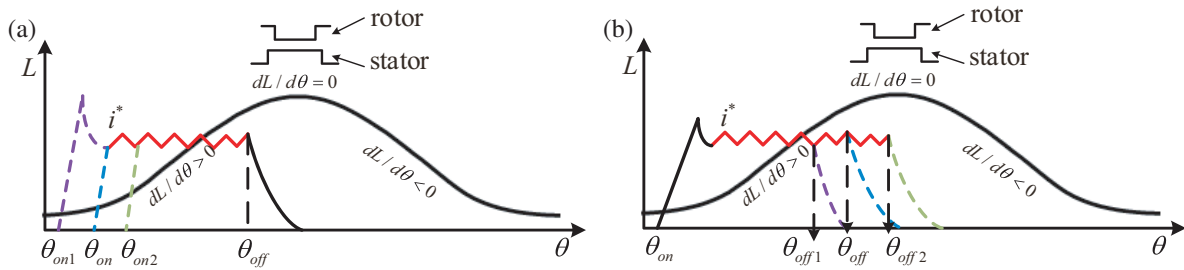
FIGURE 10. Phase current waveforms of PMa-SRM with different conduction angles.

the phase current, and θ_{on} and θ_{off} denote the turn-on and turn-off angles, respectively. From Fig. 10(a), it can be observed that advancing θ_{on1} favors the establishment of incoming phase current but increases peak current, thereby raising copper losses and reducing efficiency. Delaying θ_{on2}, however, results in insufficient incoming phase torque output, leading to inadequate composite torque and increased torque ripple.

Figure 10(b) depicts the current waveforms under fixed turn-on and varying turn-off angles. Advancing θ_{off1} may abruptly decrease incoming phase torque output, leading to increased torque ripple. Conversely, delaying θ_{off2} may extend phase current into the region of decreasing inductance, resulting in negative torque generation. Therefore, dynamic adjustment of turn-on and turn-off angles is necessary to enhance motor efficiency and reduce torque ripple.

This study employs DBO-BP to predict the turn-on and turn-off angles under various speeds and load conditions. The BP neural network is a type of error back-propagation neural network, processes information by adjusting the relationships between points, and has strong self-learning and self-adaptation abilities. The structure of the three-layer BP neural network is illustrated in Fig. 11, which contains an input layer, a hidden layer, and an output layer, and the numbers of its neurons are i, j, and k, respectively. The layers are connected by weights; ω_{ij} and ω_{jk} represent the connection weights between the input and hidden layers and between the hidden and output lay-
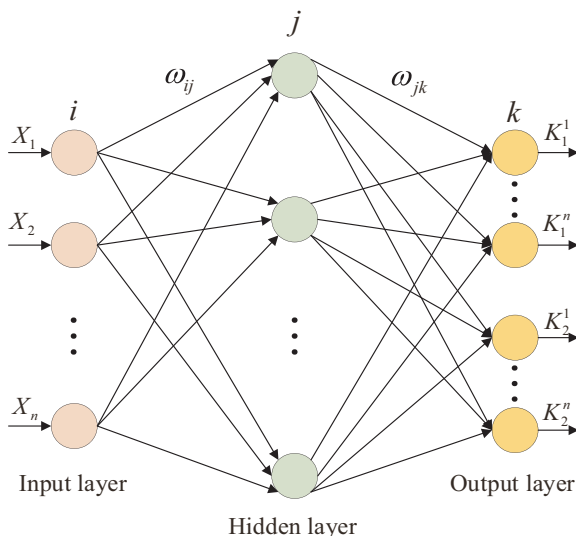
ers, respectively. After receiving information, neurons in each layer process it through an activation function before passing it to the next layer. In the output layer, the predicted values are compared to the real values, and the error between them is calculated. The output of neurons in each layer can be expressed as:

$$\begin{cases} u_i = x_i & \text{input layer} \\ u_j = f\left(\sum_{i=1}^{m} \omega_{ij} x_i + \theta_j\right) & \text{hidden layer} \\ u_k = f\left(\sum_{j=1}^{p} \omega_{jk} \cdot f\left(\sum_{i=1}^{m} \omega_{ij} x_i + \theta_j\right) + \theta_k\right) & \text{output layer} \end{cases}$$

(6)

where θ_j, θ_k, and $f(x)$ are the hidden layer threshold, output layer threshold, and activation function, respectively.

Although the BP neural network can solve nonlinear mapping problems well, it is prone to falling into local minima, which leads to insufficient prediction accuracy. The dung beetle algorithm, with its strong global search ability, compensates for the BP neural network's lack of global search capability. DBO has the characteristics of fast convergence speed and high accuracy. By optimizing the weights and thresholds of the BP neural network, it can overcome the issue of local minima and improve the prediction accuracy of the model.

In the prediction model, rotational speed and load torque are inputs to the input layer, while turn-on and turn-off angles are outputs from the output layer. To minimize torque ripple and copper losses, 100 sample data sets, as depicted in Fig. 12, are divided into 75 training sets and 25 testing sets. The DBO parameters are configured as follows: a population size of 30 beetles comprises 6 rolling beetles, 6 breeding beetles, 7 foraging beetles, and 11 thief beetles; initial optimization problem boundaries are set from −5 (lower bound) to 5 (upper bound). The fitness function is defined in MATLAB as follows:

$$\begin{aligned} f_{fitness} = \ & \arg\min(mse(TrainDateError) \\ & + mse(TestDateError)) \end{aligned}$$

(7)

where $f_{fitness}$ is the fitness function; $TrainDateError$ is the training set error; $TestDateError$ is the test set error. The flowchart of the dung beetle algorithm to optimize the BP neural network is shown in Fig. 13.

Trained DBO-BP model is used to predict the turn-on and turn-off angles, and the prediction results for 25 sets of sample data are shown in Figs. 14(a) and (b). It can be seen that the DBO-BP prediction results are very close to the actual values
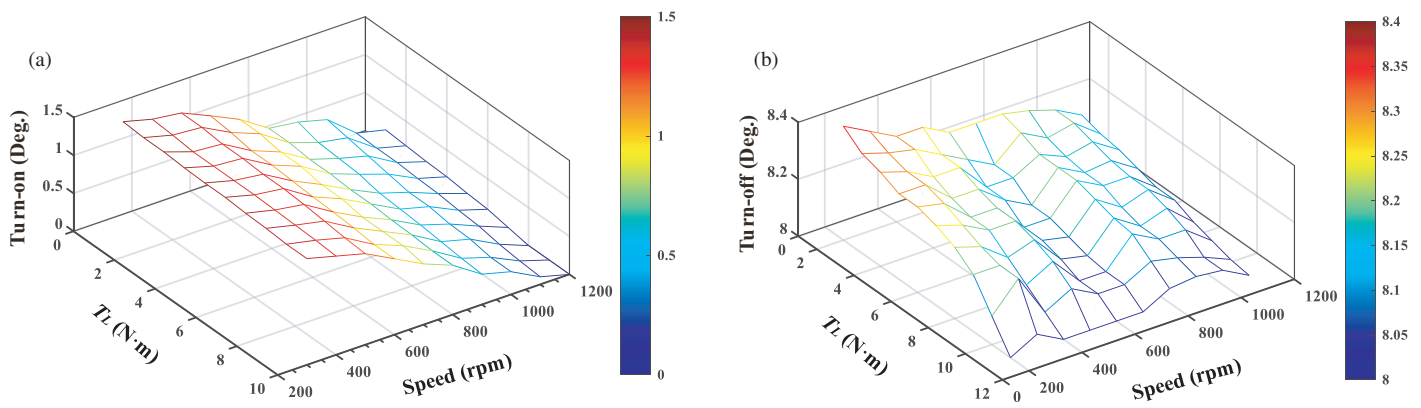

FIGURE 11. BP neural network structure.

FIGURE 12. Sample data set. (a) Turn-on angle data. (b) Turn-off angle data.
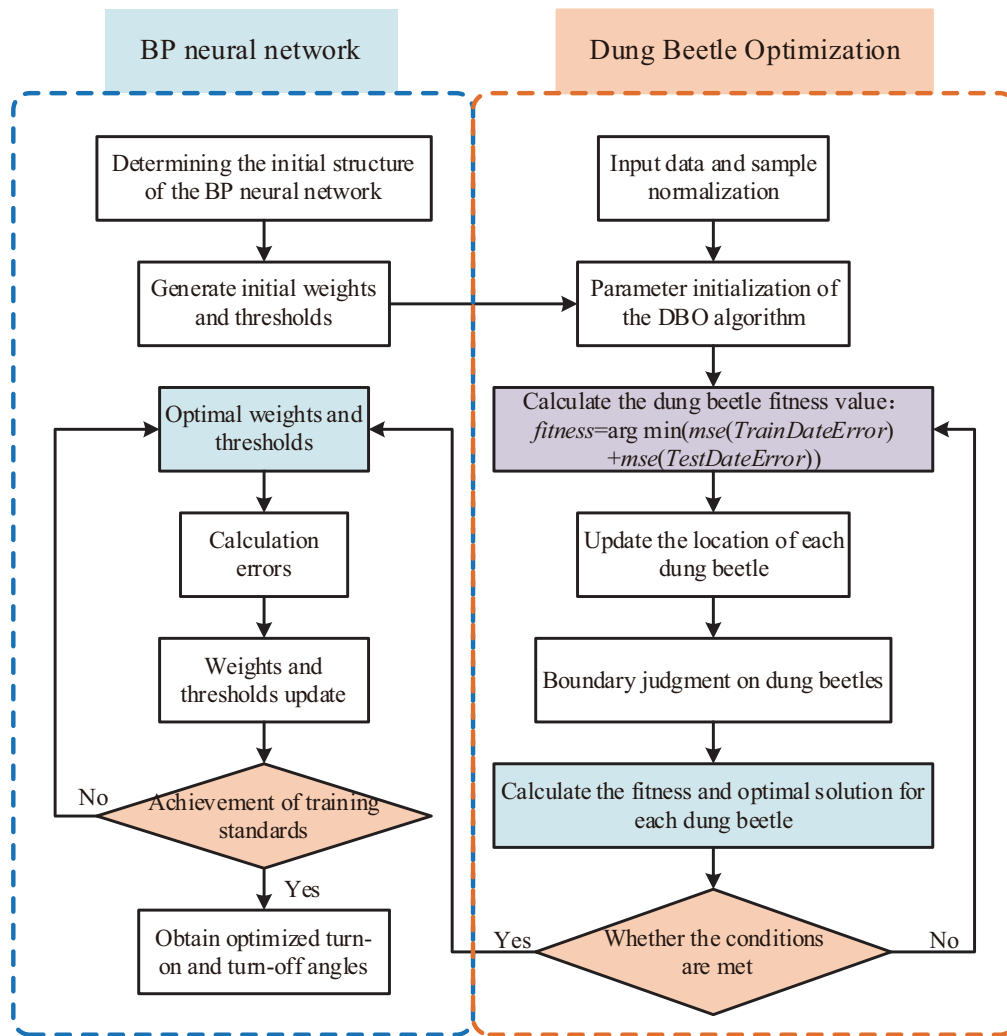

FIGURE 13. DBO-BP flow chart.

and demonstrate a good prediction effect. To verify the validity of the proposed algorithm, it is compared with PSO-BP and BP neural network models. The absolute percentage errors of the three models are shown in Fig. 14(c), which indicates that the DBO-BP model has the smallest error followed by the PSO-BP model, with the BP prediction model having the largest error.

4. SIMULATION ANALYSIS

To verify the feasibility and effectiveness of the proposed novel DITC method with zero-voltage modulation, a three-phase 6/20 pole PMa-SRM is used as a prototype to build a simulation model of the control system in the Matlab/Simulink environ-
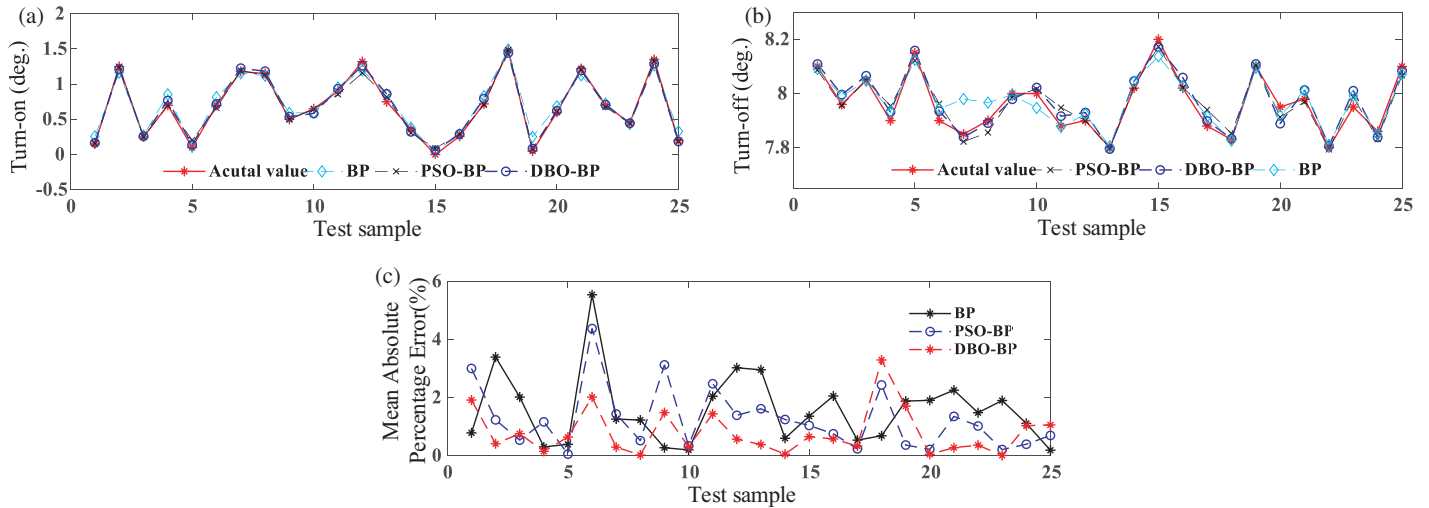
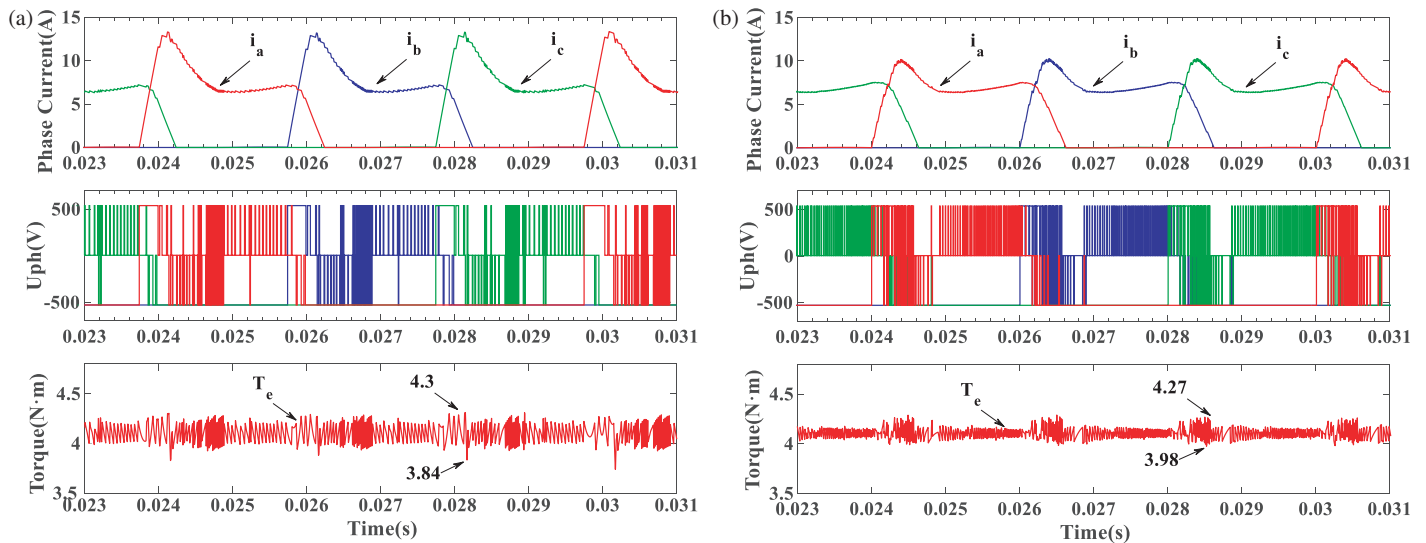**FIGURE 14**. Comparison of DBO-BP predicted and actual values.

FIGURE 15. Simulated waveforms for a load of 4 Nm and a speed of 500 rpm. (a) Conventional DITC. (b) Proposed DITC.

TABLE 1. Motor parameters.

Parameters	Values	Parameters	Values
Phase number	3	Windings turns	55
Stator poles	6	Rotor diameter/mm	172
Rotor poles	20	Stator diameter/mm	142
Max current/A	30	Rated speed/(rpm)	1500
Rated voltage/V	540	Stack length/(mm)	100

ment. The parameters of the prototype are shown in Table 1. The PWM frequency is 10 kHz in the simulation, and the torque error thresholds ΔT_{max} and ΔT_{min} are 0.2 and 0.1, respectively.

The simulation comparison between the conventional DITC method and the novel DITC method with zero voltage modulation is carried out under different operating conditions. The

torque ripple coefficient K_T is defined as:

$$K_T = \frac{T_{max} - T_{min}}{T_{avg}} \times 100\% \qquad (8)$$

where T_{max}, T_{min}, and T_{avg} are the maximum value of torque, the minimum value of torque, and the average torque, respectively.

At a reference speed of 500 rpm and a load of 4 Nm, Fig. 15 shows the current, voltage, and torque waveforms for two control strategies. The conventional DITC method results in a peak current of 13.2 A, whereas the proposed DITC method achieves a peak current of 10 A and a reduction of 3.2 A. The torque ripple percentages for the conventional and proposed DITC methods are 11.5% and 7.25%, respectively. Analysis of the voltage waveform indicates that the conventional DITC, which uses hysteresis band rules for signal output, leads to variable switching frequencies and larger torque ripples. In contrast, the proposed DITC method uses fixed-frequency PWM for signal out-
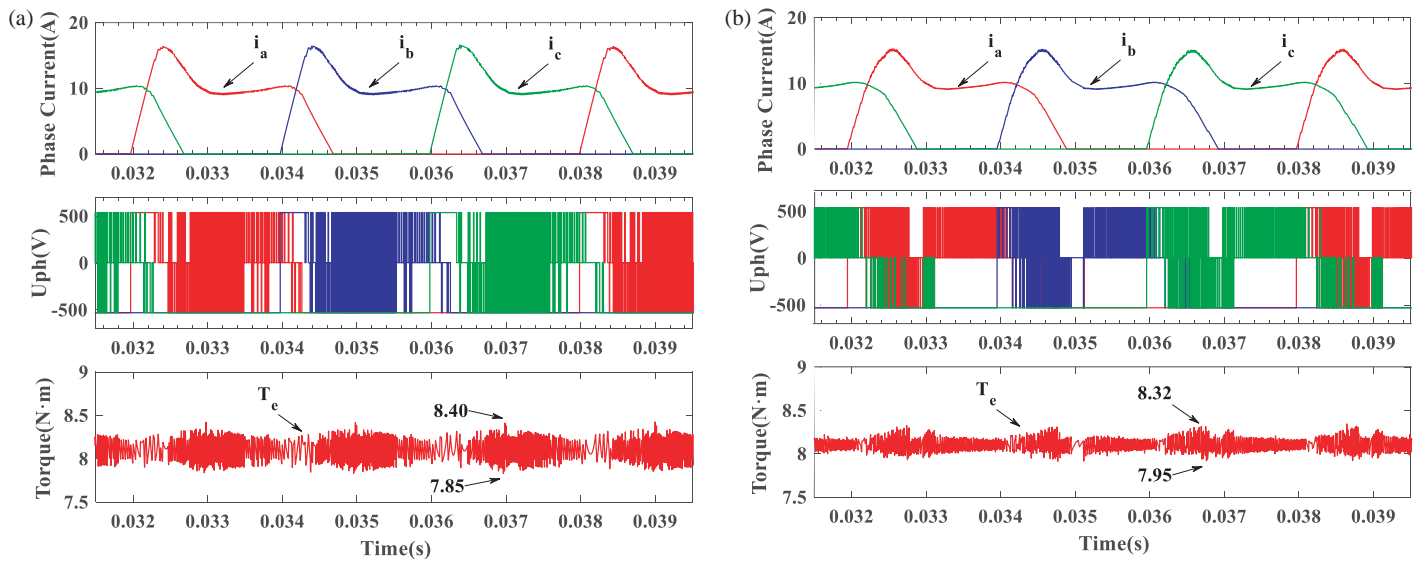
FIGURE 16. Simulated waveforms for a load of 8 Nm and a speed of 500 rpm. (a) Conventional DITC. (b) Proposed DITC.
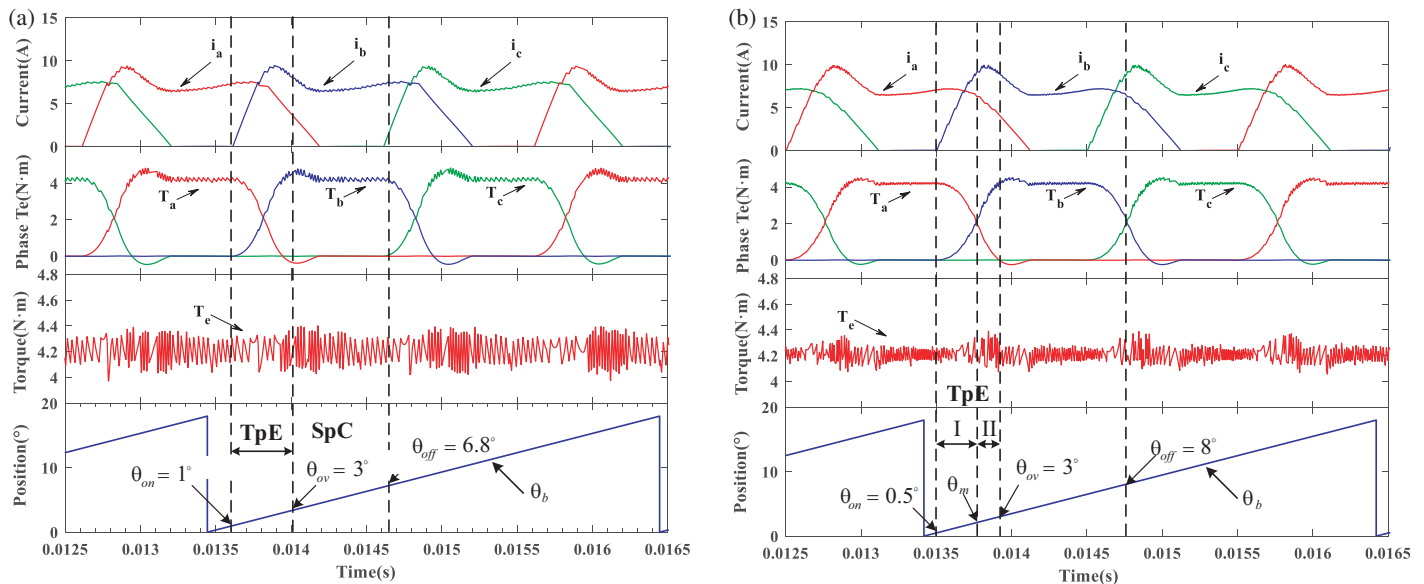

FIGURE 17. Simulated waveforms for a load of 4 Nm and a speed of 1000 rpm. (a) Conventional DITC. (b) Proposed DITC.

put control and adaptively adjusts the duty cycle across different intervals to regulate winding terminal voltages. This approach effectively reduces torque ripple and enhances overall efficiency.

Figure 16 presents the current, voltage, and torque waveforms for two control methods at a speed of 500 rpm and an increased load of 8 Nm. The peak current for the conventional DITC is 16.3 A, while the proposed DITC achieves a peak current of 15 A, resulting in torque ripples of 10.875% and 4.625%, respectively. The proposed DITC demonstrates reductions in both peak current and torque ripple. Analysis of the voltage waveform in Fig. 16 indicates that the proposed DITC, which utilizes zero-voltage modulation, reduces the number of voltage pulses compared to the conventional DITC. This reduction

in pulse frequency leads to decreased switching losses in the components.

When the speed is increased to 1000 rpm with a load of 4 Nm, the phase current, phase torque, and position angle waveforms for two control strategies are shown in Fig. 17. The conventional DITC method features a turn-on angle of 1° and a turn-off angle of 6.8°, whereas the proposed DITC has a turn-on angle of 0.5° and a turn-off angle of 8°. The conventional DITC method exhibits significant torque ripple in the commutation region. In contrast, the proposed DITC method employs segmented control based on TCR, which effectively suppresses torque ripple within this region.

As depicted in Fig. 18, at a speed of 1000 rpm with a load of 8 Nm, the fixed turn-on and turn-off angles of the conventional DITC result in a sudden increase in torque ripple within
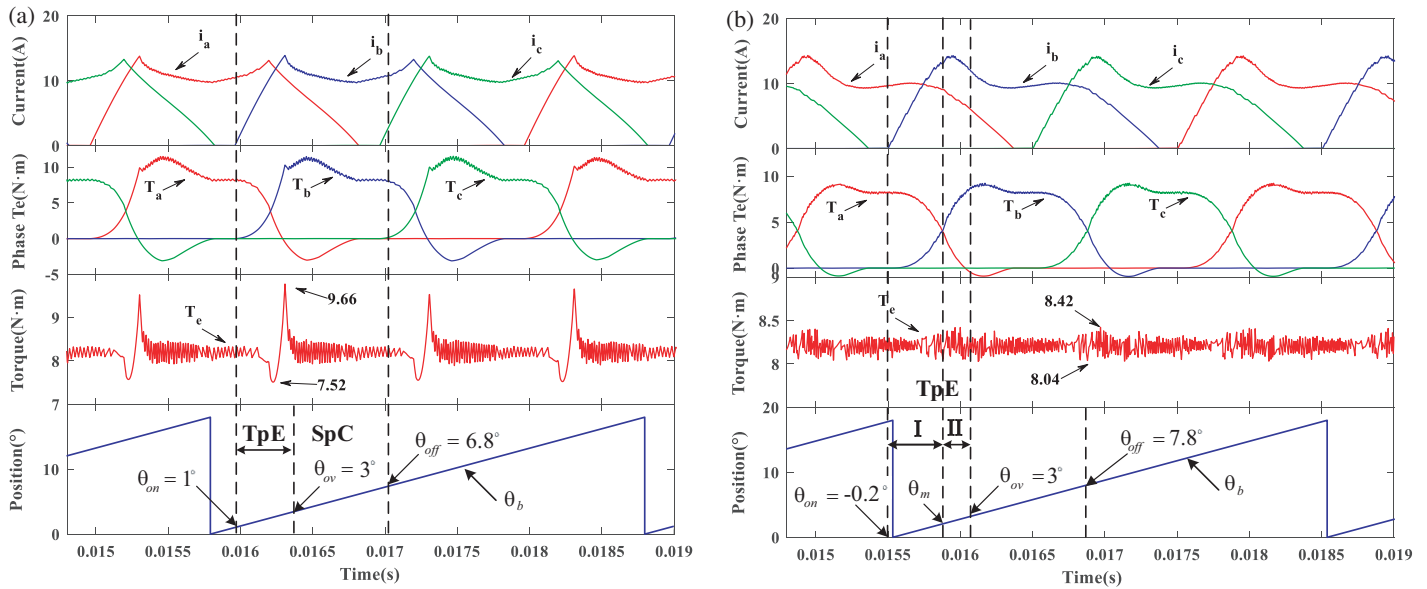
FIGURE 18. Simulated waveforms for a load of 8 Nm and a speed of 1000 rpm. (a) Conventional DITC. (b) Proposed DITC.

the commutation region, reaching 26.75%. In contrast, the proposed DITC, which is optimized for conduction angle substantially reduces torque ripple to 4.75%. The turn-on and turn-off angles are adjusted to $-0.2°$ and $7.8°$, respectively. The phase torque waveform in Fig. 18 clearly shows that the conventional DITC method results in greater negative torque and increased composite torque ripple. Conversely, the proposed DITC method, with its segmented control and optimized conduction angles, effectively minimizes both negative torque and overall torque ripple.

To further validate the effectiveness of the proposed zero-voltage modulation DITC method, simulations were conducted comparing conventional PWM control, conventional DITC, and the proposed method under different operating conditions. Table 2 presents quantitative analyses of torque ripple and peak current for each control method. The traditional PWM control cannot operate under high-speed and high-load conditions. Although conventional DITC can operate, it exhibits torque ripple reaching 106.5%. In contrast, the proposed control method consistently shows lower torque ripple and peak current under both low-speed, low-load and high-speed, high-load conditions than the other two methods.

TABLE 2. Simulation comparison of different control strategies.

Method	Speed (rpm)	T_L (Nm)	T_r (%)	I_{max} (A)
Conventional DITC	600	5	10.2	13
Conventional PWM	600	5	19.6	12
Proposed method	600	5	6.4	11.5
Conventional DITC	1200	10	106.5	15.2
Conventional PWM	1200	10	×	×
Proposed method	1200	10	6.7	15

5. EXPERIMENTAL VALIDATION

The control system was implemented using the TI TMS320F28335 microcontroller, as depicted in Fig. 19 of the experimental platform. A three-phase 6/20 pole PMa-SRM with parameters identical to the simulation was driven by an AHBC circuit. PWM drive signals were generated by a DSP control board. To enhance control precision, both the switch frequency and DSP sampling frequency were set to 10 kHz. The load torque was applied by an electromagnetic powder brake, and torque signals were measured using a torque transducer.
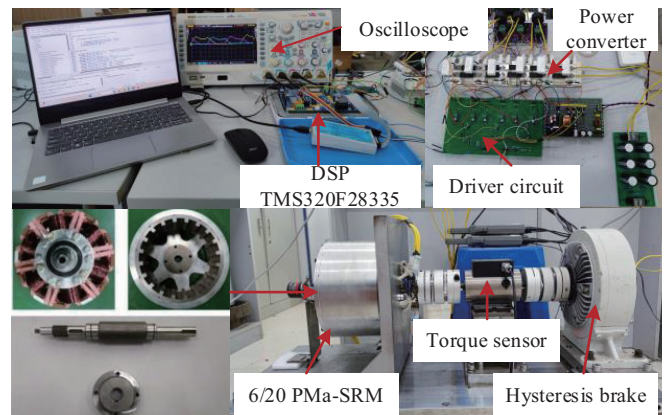

FIGURE 19. Experimental platform for motor drive system.

Figure 20 shows the experimental results of the two control strategies at a speed of 500 r/min and a load of 4 Nm. The current waveform indicates that the peak current for the conventional DITC strategy is 13.5 A, while for the proposed DITC method, it is 10 A. Thus, the peak current of the proposed method is reduced by 3.5 A due to the optimized conduction angle, which improves motor efficiency. Regarding the torque
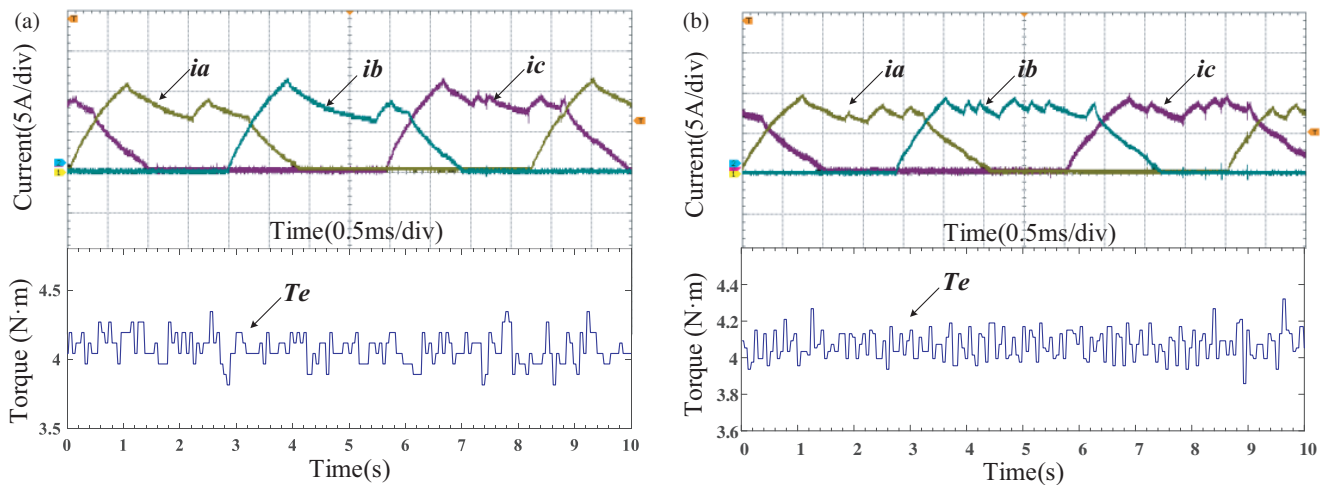
FIGURE 20. Experimental results for speed of 500 rpm and load of 4 Nm. (a) Conventional DITC. (b) Proposed DITC.
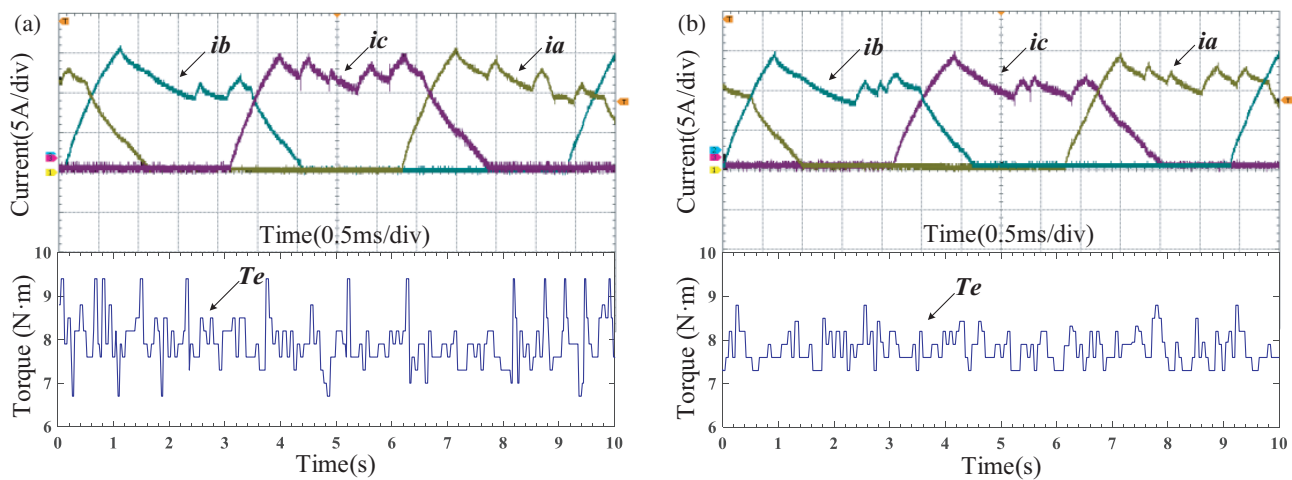

FIGURE 21. Experimental results for speed of 500 rpm and load of 8 Nm. (a) Conventional DITC. (b) Proposed DITC.

waveform, limited experimental conditions and insufficient acquisition accuracy of the torque sensor resulted in fewer data points. Additionally, measurement hysteresis caused a long response time, leading to discrepancies between experimental and simulated results. The conventional DITC strategy exhibits a significant torque ripple of 18.65%, whereas the proposed DITC strategy, utilizing a zero-voltage decentralized modulation method, effectively suppresses the torque ripple to 10%.

To validate the proposed method, loading experiments were performed on the PMa-SRM. Fig. 21 shows waveforms at 500 rpm with an 8 Nm load. With the conventional DITC, torque performance worsens as the load increases, resulting in a torque ripple of 33.75% and a peak current of 16.5 A. In contrast, the proposed method reduces torque ripple to 18.75% and peak current to 15 A, demonstrating improved stability. The new method also enhances motor efficiency and reduces copper losses through optimized conduction angles. The torque ripple in the experiment is higher than in the simulation results because the current sensor is affected by electromagnetic interference, which leads to a larger error in the feedback signal.

Although there are some differences between the experimental results and simulated ones, the experiment demonstrates the effectiveness of the proposed method.

6. CONCLUSION

This paper addresses the problems of unfixed switching frequency and large torque ripple in the conventional DITC method. Fixed-frequency PWM control is used instead of the hysteresis loop controller, and the TpE region is controlled in intervals according to the inductance and TCR characteristics, while the conduction angle is optimized to improve the motor performance. The following conclusions are drawn from the simulation and experimental comparative analysis:

1) The zero-voltage decentralized modulation method can increase the number of voltage pulses and reduce the switching loss without increasing the switching frequency. Combined with the TCR characteristic adaptive control of the duty cycle in different regions, it can improve the torque tracking performance and realize the suppression of torque ripple.

2) Optimizing the turn-on and turn-off angles under varying operating conditions using DBO-BP minimizes peak phase currents enhances efficiency, and further reduces torque ripple.

REFERENCES

[1] Farahani, E. F., M. A. J. Kondelaji, and M. Mirsalim, "A new exterior-rotor multiple teeth switched reluctance motor with embedded permanent magnets for torque enhancement," *IEEE Transactions on Magnetics*, Vol. 56, No. 2, 1–5, 2020.

[2] Ding, W., H. Fu, and Y. Hu, "Characteristics assessment and comparative study of a segmented-stator permanent-magnet hybrid-excitation SRM drive with high-torque capability," *IEEE Transactions on Power Electronics*, Vol. 33, No. 1, 482–500, 2017.

[3] Huang, C. Z., J. Xu, and X. P. Liu, "A four-interval DITC method for permanent magnet assisted switched reluctance motor," *Proceedings of the CESS*, Vol. 43, No. 06, 2438–2450, 2023.

[4] Diao, K., X. Sun, G. Lei, Y. Guo, and J. Zhu, "Multiobjective system level optimization method for switched reluctance motor drive systems using finite-element model," *IEEE Transactions on Industrial Electronics*, Vol. 67, No. 12, 10 055–10 064, 2020.

[5] Lan, Y., Y. Benomar, K. Deepak, A. Aksoz, M. E. Baghdadi, E. Bostanci, and O. Hegazy, "Switched reluctance motors and drive systems for electric vehicle powertrains: State of the art analysis and future trends," *Energies*, Vol. 14, No. 8, 2079, 2021.

[6] Sun, X., J. Wu, G. Lei, Y. Guo, and J. Zhu, "Torque ripple reduction of SRM drive using improved direct torque control with sliding mode controller and observer," *IEEE Transactions on Industrial Electronics*, Vol. 68, No. 10, 9334–9345, 2021.

[7] Huang, C., W. Cao, and J. Xu, "An NUTSF at sub-region for suppression of torque ripple in switched reluctance motors," *Applied Sciences*, Vol. 12, No. 15, 7604, 2022.

[8] Yu, Z., C. Gan, K. Ni, Y. Chen, and R. Qu, "A simplified PWM strategy for open-winding flux modulated doubly-salient reluctance motor drives with switching action minimization," *IEEE Transactions on Industrial Electronics*, Vol. 70, No. 3, 2241–2253, 2023.

[9] Sun, Q., J. Wu, and C. Gan, "Optimized direct instantaneous torque control for SRMs with efficiency improvement," *IEEE Transactions on Industrial Electronics*, Vol. 68, No. 3, 2072–2082, 2020.

[10] Cao, X., H. Hu, N. Yan, and Z. Deng, "Direct torque control of switched reluctance motor with real-time optimization of sectors," *Transactions of China Electrotechnical Society*, Vol. 33, No. 19, 4526–4534, 2018.

[11] Yang, F., H. Chen, V. Pires, J. Martins, Y. Gorbounov, X. Li, and M. Orabi, "Improved direct torque control strategy for reducing torque ripple in switched reluctance motors," *Journal of Power Electronics*, Vol. 22, No. 4, 603–613, 2022.

[12] Huang, C., W. Cao, Y. Sun, Z. Chen, and W. Zhang, "A control method of switched reluctance motor based on non-unity TSF and adaptive overlapping angle," *Progress In Electromagnetics Research C*, Vol. 133, 233–249, 2023.

[13] Xia, Z., G. Fang, D. Xiao, A. Emadi, and B. Bilgin, "An online torque sharing function method involving current dynamics for switched reluctance motor drives," *IEEE Transactions on Transportation Electrification*, Vol. 9, No. 1, 534–548, 2023.

[14] Genc, U. and B. Tekgun, "Instantaneous torque error compensation based online torque sharing function for switched reluctance machines," *Alexandria Engineering Journal*, Vol. 75, 261–270, 2023.

[15] Xia, Z., B. Bilgin, S. Nalakath, and A. Emadi, "A new torque sharing function method for switched reluctance machines with lower current tracking error," *IEEE Transactions on Industrial Electronics*, Vol. 68, No. 11, 10 612–10 622, 2021.

[16] Cai, Y., C. Ju, H. Wang, Y. Wan, and H. Zhang, "A new direct instantaneous torque control method of switched reluctance motor," *Transactions of China Electrontechnical Society*, Vol. 37, No. 18, 4625–4637, 2022.

[17] Sun, Q., J. Wu, and C. Gan, "Optimized direct instantaneous torque control for SRMs with efficiency improvement," *IEEE Transactions on Industrial Electronics*, Vol. 68, No. 3, 2072–2082, 2021.

[18] Huang, C., W. Cao, Z. Chen, Y. Wu, and Y. Geng, "An improved DITC control method based on turn-on angle optimization," *CES Transactions on Electrical Machines and Systems*, Vol. 7, No. 4, 379–389, 2023.

[19] Song, S., G. Fang, R. Hei, J. Jiang, R. Ma, and W. Liu, "Torque ripple and efficiency online optimization of switched reluctance machine based on torque per ampere characteristics," *IEEE Transactions on Power Electronics*, Vol. 35, No. 9, 9608–9616, 2020.

[20] Huang, C., Y. Wu, W. Cao, Z. Zhu, and Y. Geng, "A three-interval PWM duty cycle adaptive method for torque ripple suppression of switched reluctance motor," *Progress In Electromagnetics Research M*, Vol. 111, 103–117, 2022.

[21] Wang, S., Z. Hu, and X. Cui, "Research on novel direct instantaneous torque control strategy for switched reluctance motor," *IEEE Access*, Vol. 8, 66 910–66 916, 2020.

[22] Zhu, Y., G. Zhang, and Y. Huang, "PWM-based direct instantaneous torque control of switched reluctance machine," *Transactions of China Electrotechnical Society*, Vol. 32, No. 7, 31–39, 2017.

[23] Zhang, M., H. Xie, W. Hu, J. Li, Q. Huang, and R. Zhou, "A vibration reduction method based on smooth voltage PWM control of switched reluctance machines," *Energy Reports*, Vol. 8, 1398–1405, 2022.